

Visual Control for Multi-Robot Organized Rendezvous

G. López-Nicolás, *Member, IEEE*, M. Aranda, *Student Member, IEEE*, Y. Mezouar, *Member, IEEE* and C. Sagüés, *Senior Member, IEEE*

Abstract—This paper addresses the problem of visual control of a set of mobile robots. In our framework, the perception system consists of an uncalibrated flying camera performing an unknown general motion. The robots are assumed to undergo planar motion considering nonholonomic constraints. The goal of the control task is to drive the multi-robot system to a desired rendezvous configuration relying solely on visual information given by the flying camera. The desired multi-robot configuration is defined with an image of the set of robots in that configuration without any additional information. We propose a homography-based framework relying on the homography induced by the multi-robot system, that gives a desired homography to be used to define the reference target, and a new image-based control law that drives the robots to the desired configuration by imposing a rigidity constraint. This paper extends our previous work and the main contributions are that the motion constraints on the flying camera are removed, the control law is improved by reducing the number of required steps, the stability of the new control law is proved, and real experiments are provided to validate the proposal.

Index Terms—Multiple mobile robots, visual control, homography, formation.

I. INTRODUCTION

Nowadays, multi-robot systems are an important research area in robotics. It is known that a multi-robot system can perform tasks that are difficult for one single robot such as exploration, surveillance, security or rescue applications. One of the research topics in this area deals with the problem of maintaining the robot team in a particular configuration. Different issues can be tackled within this topic, such as navigation in formation [1], flocking of multiple robots [2], or path following in formation [3]. Some other related works are the leader-follower approach in [4], where the orientation deviations between the leaders and followers are explicitly controlled; [5], where consensus algorithms are used for rendezvous and formation control of multiple robots; or [6] where limited information constraints are considered.

G. López-Nicolás, M. Aranda and C. Sagüés are with Instituto de Investigación en Ingeniería de Aragón. Universidad de Zaragoza, 50018 Zaragoza, Spain.

gonlopez@unizar.es, marandac@unizar.es, csagues@unizar.es
Y. Mezouar is with Clermont Université, Université Blaise Pascal, Institut Pascal, BP 10448, F-63000 Clermont-Ferrand; and with CNRS, UMR 6602, Institut Pascal, F-63177 Aubiere, France.

mezouar@univ-bpclermont.fr

This paper has supplementary downloadable material available at <http://ieeexplore.ieee.org>, provided by the authors. This includes three movie clips, which illustrate the experimental results.

This work was supported by Ministerio de Ciencia e Innovación/Unión Europea, DPI2009-08126, grant AP2009-3430 Ministerio de Educación, ANR projects R-Discover and grant (code I09200) from Gyeonggi Technology Development Program funded by Gyeonggi Province.

In this work, we considered a framework with a centralized setup. By now, the various tradeoffs and shortcomings of centralized and decentralized approaches have been investigated [4], [7], [8], [9], [10]. Some of the advantages of adopting a centralized approach is that it allows to use simple and cheap robots, and releases their local resources transferring expensive computations to an external computer.

Vision has been extensively used for robot localization, navigation and control [11]. Visual control is an extensive field of research in the design of motion controllers and it has focused the attention of many researchers [12], [13]. Some examples of the application of vision to tasks performed by multiple mobile robots are the localization method presented in [14], the vision-based formation control with feedback-linearization in [7] or for robot coordination [9]. Another related work is [15], that aims to enable groups of mobile robots to visually maintain formations in the absence of communication.

In general, visual information is more robust if multiple view geometry constraints are imposed [16], [17]. The homography is a well-known geometric model across two views induced by a plane of the scene, that has been used often for visual control [18], [19], [20], [21]. Here, we propose a homography-based control approach that takes advantage of the planar motion constraint of the nonholonomic robots to parameterize the homography. The visual information is acquired by a flying camera performing an unknown arbitrary general motion, and the image features used to compute the homography are the projection of the multiple robots on the image plane. The goal of the task to fulfill is to drive the multiple robots to a desired rendezvous configuration defined by an image previously taken of that configuration. In this framework, the computed homography gives information about the actual configuration of the set of robots. In particular, it can be known if the motion performed by the robots is rigid, i.e. they maintain the desired configuration defined by the reference image, or nonrigid, meaning that the robots are in a different configuration to the one desired. To our knowledge, this is the first time the homography model is proposed for visual control of a multi-robot system. Unlike classical approaches with individual robots, here the homography is not decomposed to get pose parameters of the system. For instance, approaches based on pose information can be found in [3], [22]. Our proposed image-based control scheme avoids the need of camera calibration of position-based approaches.

Some drawbacks of classical image-based approaches are the singularities of the interaction matrix, local minima and the

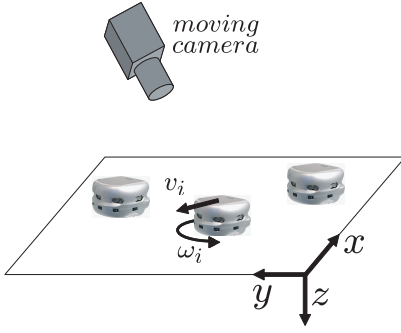


Fig. 1. Multi-robot and camera framework: The robots undergo planar motion in the $x-y$ plane of the global reference and the camera performs an unknown general motion.

difficulty of taking into account the nonholonomic constraints of the robotic platforms. In order to solve the task considered and overcome these issues, a new image-based control law using an uncalibrated flying camera is proposed, in which a desired homography is defined as a reference for the control so as to drive the robots to the desired configuration. Notice that classical image-based approaches cannot be used directly in our framework, since we essentially work with image information that consists of a nonrigid scene.

In our previous paper [23], we presented the homography-based framework, that provides a homography constraint to be used to define the reference target, and an image-based control law that drives the robots to the desired configuration. In that work, the flying calibrated camera was constrained to a planar motion, in such a way that its translation was parallel to the robot's plane of motion and the rotation was parallel to the plane normal. Here, the camera motion is not constrained and as a result, the uncalibrated camera can perform any 3D motion. We now extend the work of [23] with the following contributions: The flying camera motion constraints are removed with a new target homography computation procedure; The control law is also improved by reducing the number of required steps to fulfill the task and the stability analysis is also provided; In addition, the proposal is tested in real experiments with a set of robots. The advantages of the approach presented are that any arbitrary desired configuration can be easily defined with one image, avoiding the need of additional information except for the computation of the line at infinity and the circular points. Another advantage of our approach is that unknown general arbitrary camera motion is allowed without affecting the control performance.

The paper is organized as follows. Section II presents the image information processed for the parametrization of the homography and the definition of the desired homography for reaching the multi-robot rendezvous configuration. The control law for the multi-robot system is presented in section III including the stability analysis of the control scheme. Simulations and real experiments are given in Section IV to illustrate the performance of the proposed approach.

II. HOMOGRAPHY-BASED SCHEME

The setup of the multi-robot system and the flying camera is illustrated in Fig. 1, where the global fixed left-handed

coordinate system is depicted. In the following, we introduce the homography and describe the method to linearly compute the homography from only two correspondences by taking advantage of the parametrization obtained after performing image rectification. Finally, we define the target homography that corresponds to the the desired configuration of the multi-robot system. This target homography is used as control reference in Section III.

A. The Homography

Two perspective images can be geometrically linked through a plane by a homography $\mathbf{H}_u \in \mathbb{R}^{3 \times 3}$, where subindex u stands for uncalibrated. This projective transformation \mathbf{H}_u relates points of the plane projected in both images. Pairs of corresponding points $(\mathbf{p}_u, \mathbf{p}'_u)$ are then related up to scale by $\mathbf{p}'_u = \mathbf{H}_u \mathbf{p}_u$, where the point coordinates are given in pixels and the homography is uncalibrated. The point coordinates can be transformed into a calibrated retina by using the intrinsic camera calibration encapsulated by matrix $\mathbf{K} \in \mathbb{R}^{3 \times 3}$ [24] by means of the expressions $\mathbf{p}_c = \mathbf{K}^{-1} \mathbf{p}_u$ and $\mathbf{p}'_c = \mathbf{K}^{-1} \mathbf{p}'_u$, where subindex c stands for calibrated. Then, the calibrated homography \mathbf{H}_c relates corresponding calibrated points up to scale by $\mathbf{p}'_c = \mathbf{H}_c \mathbf{p}_c$ and it is related with the uncalibrated homography: $\mathbf{H}_c = \mathbf{K}^{-1} \mathbf{H}_u \mathbf{K}$. The calibrated homography can be related to camera motion and plane parameters as follows:

$$\mathbf{H}_c = \mathbf{R} + \mathbf{T} \mathbf{n}^T / d, \quad (1)$$

where $\mathbf{R} \in \mathbb{R}^{3 \times 3}$ and $\mathbf{T} \in \mathbb{R}^3$ are respectively the relative rotation and translation of the camera, $\mathbf{n} \in \mathbb{R}^3$ is the unit normal of the plane with respect to the reference camera frame and d is the distance along \mathbf{n} between the plane and the reference position.

In our framework, the mobile robots move in a planar surface that generates the homography. We also let the camera to undergo a general 3D motion instead of constraining its motion to be parallel to this planar surface, as in [23]. Notice that the distance d is the height of the camera with respect to the motion plane of the robots. In this framework, the uncalibrated homography matrix is given by

$$\mathbf{H}_u = \begin{bmatrix} h_{11} & h_{12} & h_{13} \\ h_{21} & h_{22} & h_{23} \\ h_{31} & h_{32} & h_{33} \end{bmatrix}, \quad (2)$$

which is the general form of a projective transformation. Hereafter, and unlike in [23], the camera calibration matrix \mathbf{K} is unknown and not computed. Thus, the image information is used in uncalibrated coordinates leading to the uncalibrated homography \mathbf{H}_u .

B. Multi-Robot Image Rectification

The projection of the robot formation on the image depends on the actual multi-robot configuration and the motion of the camera. The approach proposed needs to abstract the information of the multi-robot formation from the camera motion effects. This is done through a particular parametrization of the homography. However, to succeed, the productivity

encapsulated by the homography needs to be generated only from the relative motion of the robots. Then, the camera motion is required to affect the homography only up to a similarity transformation. This condition is met in [23] by constraining the motion of the camera to a parallel plane with respect to the robot's plane of motion, maintaining a constant height. Here, the camera undergoes a general motion, and in this case, there is an ambiguity with respect to the scale factor: it is not possible to distinguish an expansion/contraction of the robot formation from the camera moving towards or away from the robots. In order to solve this issue the acquired images are rectified before carrying out the homography and control computations presented in the following sections.

Different methods can be used to remove projective and affine distortions from images. Affine rectification was used in [25] for the problem of matching of planar structures. That method is based on the detection of the vanishing line of the plane for reducing the transformation from world to image plane to an affinity. The rectification of the image can be stratified in two steps: first the affine properties and then the metric properties are recovered [26]. A rectification procedure is investigated in [27] describing how to recover affinity from parallel lines and metric properties from known angles in the plane by using automatic detection of vanishing points and orthogonal directions. The rectification process is carried out in [28] by estimating the image of the absolute conic based on the identification of circles in the image.

Here we follow the procedure presented in [27], which is also described in [24], for the rectification of the images to a similarity transformation. The rectification is performed in two steps. In the first step, parallel lines are identified to compute the line at infinity $\mathbf{l} = (l_1, l_2, l_3)^T$ that will be mapped to $\mathbf{l}_\infty = (0, 0, 1)^T$. The line at infinity is used for the affine rectification of the image points using expressions $\mathbf{p}_A = \mathbf{H}_A \mathbf{p}_u$ and $\mathbf{p}'_A = \mathbf{H}_A \mathbf{p}'_u$ with the matrix \mathbf{H}_A defined as

$$\mathbf{H}_A = \begin{bmatrix} 1 & 0 & 0 \\ 0 & 1 & 0 \\ l_1 & l_2 & l_3 \end{bmatrix}. \quad (3)$$

In the second step, the circular points are determined from imaged orthogonal lines on the world plane and the image is rectified to a similarity. The expressions that map the points to a similarity are $\mathbf{p}_S = \mathbf{H}_S \mathbf{p}_A$ and $\mathbf{p}'_S = \mathbf{H}_S \mathbf{p}'_A$, where the matrix \mathbf{H}_S can be written as

$$\mathbf{H}_S = \begin{bmatrix} s_{11} & s_{12} & 0 \\ s_{21} & s_{22} & 0 \\ 0 & 0 & 1 \end{bmatrix}. \quad (4)$$

This corresponds to a similarity, which is a symmetric matrix compounded by a rotation and isotropic scaling. The visual information of each image is given up to an unknown scale and, finally, we seek a common scale transforming the point coordinates with $\mathbf{p} = \mathbf{H}_E \mathbf{p}_S$ and $\mathbf{p}' = \mathbf{H}_E \mathbf{p}'_S$ being \mathbf{H}_E defined as

$$\mathbf{H}_E = \begin{bmatrix} s_0 & 0 & 0 \\ 0 & s_0 & 0 \\ 0 & 0 & 1 \end{bmatrix}. \quad (5)$$

The parameter s_0 is the relative scale factor across the two images under a similarity transformation. The value of s_0 can be computed from direct comparison of the length of any common feature on the images in pixels units. Note that no metric information of the scene is required in this procedure. Therefore, the application of transformations (3), (4) and (5) to the homography gives

$$\mathbf{H} = \mathbf{H}_A^{-1} \mathbf{H}_S^{-1} \mathbf{H}_E^{-1} \mathbf{H}_u \mathbf{H}_E \mathbf{H}_S \mathbf{H}_A. \quad (6)$$

which is a matrix of the form

$$\mathbf{H} = \begin{bmatrix} h_{11} & h_{12} & h_{13} \\ h_{21} & h_{22} & h_{23} \\ 0 & 0 & h_{33} \end{bmatrix}, \quad (7)$$

where $h_{33} = 1$ and the upper left hand 2×2 matrix is given by

$$\begin{bmatrix} h_{11} & h_{12} \\ h_{21} & h_{22} \end{bmatrix} = \begin{bmatrix} \cos \theta & \sin \theta \\ -\sin \theta & \cos \theta \end{bmatrix}. \quad (8)$$

The variable θ is a relative angle that encapsulates the relative rotation of the camera and the multi-robot formation. This previous matrix (7) is the result of the rectification of the homography by removing the different distortions of the general case, corresponding to a projective transformation, leading to the particular expression (7)-(8).

C. Homography Computation from Two Points

In the framework considered here, the robots are projected in the image plane and represented by one point per robot. These points are the image features used to compute the homographies. Next, the procedure to compute the homography \mathbf{H} from point correspondences of the rectified images is described. The uncalibrated homography \mathbf{H}_u is a projective transformation that relates points of the plane projected in both images up to scale. After the rectification described in the previous section, the point correspondences are related as $\mathbf{p}' = \mathbf{H} \mathbf{p}$. The mobile robots move in a planar surface and form the plane that generates the homography. Following the procedure previously described, the transformed images are related by a homography which is conjugate to a planar Euclidean transformation given by (7). This transformation produces a translation and rotation and preserves lengths and angles.

The general homography matrix \mathbf{H}_u across two views contains nine entries, but it is defined up to a scale. Therefore, it has a number of eight degrees of freedom. Given that each point correspondence accounts for two constraints, the general projective homography \mathbf{H}_u can be computed from a minimal set of four point correspondences solving a linear system [24]. In our case, the homography has been rectified to the particular expression of (7), which contains seven entries that are not null. Again, the homography is defined up to a scale and, additionally, the constraints on (7)-(8) lead to a number of three degrees of freedom. Since each point correspondence provides two constraints, the particular homography \mathbf{H} can be computed from a minimal set of two point correspondences solving a linear system, as presented in the following.

The points considered consist of the projection of the robots on the image plane, and are denoted in homogeneous coordinates by $\mathbf{p} = (p_x, p_y, 1)$. As said before, a point correspondence $(\mathbf{p}, \mathbf{p}')$ is related up to scale by the homography as $\mathbf{p}' = \mathbf{H}\mathbf{p}$, which can be expressed in terms of the vector cross product as $\mathbf{p}' \times \mathbf{H}\mathbf{p} = \mathbf{0}$. From this expression, two linearly independent equations in the entries of \mathbf{H} (7) are obtained:

$$\begin{bmatrix} p_x & p_y & 1 & 0 & -p'_x \\ p_y & -p_x & 0 & 1 & -p'_y \end{bmatrix} \begin{pmatrix} h_{11} \\ h_{12} \\ h_{13} \\ h_{23} \\ h_{33} \end{pmatrix} = 0. \quad (9)$$

As mentioned, each point correspondence gives two independent equations. Given that \mathbf{H} is defined by seven unknown entries, and using the homography constraints $h_{11} = h_{22}$ and $h_{21} = -h_{12}$, a set of two point correspondences allows to determine the homography up to a scale factor by solving a linear system. Since h_{33} is never zero because of the particular form of (7), the scale of the homography can always be normalized and fixed by this entry.

D. The Target Homography

Each pair of robots induces a homography across two images, the current image and the image of the desired configuration. Given a set of N robots, the number of homographies defined by the different pairs of robots is $N(N-1)/2$. When the robots are in formation, the relative motion of the robots within the formation with respect to the desired configuration is rigid, i.e. the robots are in the same configuration as in the target image. In this case, one homography encapsulates the multi-robot formation, and all the homographies induced by the different pairs of robots are equal. Otherwise, when the robots are not in the desired formation, the relative motion of the set of robots with respect to the desired configuration is not rigid. In this case, different pairs of robots induce different homographies. The goal is to define a target homography induced by the robot set, by solving the linear system (9) with all the robots simultaneously, in order to lead them to the desired rendezvous configuration.

In the case in which the robots are in the desired configuration, the homography induced by the plane of the robots in formation is conjugate to a planar Euclidean transformation given by

$$\mathbf{H}_{rigid} = \begin{bmatrix} \cos \theta & \sin \theta & h_{13} \\ -\sin \theta & \cos \theta & h_{23} \\ 0 & 0 & 1 \end{bmatrix}. \quad (10)$$

A real square matrix is orthogonal if and only if its rows (or columns) form an orthonormal basis of \mathbb{R}^n . Thus, notice that the upper left hand 2×2 matrix is orthogonal. The Euclidean transformation produces a translation and rotation of the image, and preserves lengths and angles. We also have that the angle of rotation is encapsulated in the eigenvalues of (10) given by $\{1, e^{i\theta}, e^{-i\theta}\}$.

The matrix (10) corresponds to homography (7), being coherent with a rigid scene. This means that the relative motion of the robots within the formation between the current and

desired configuration is the same, i.e. the formation is rigid with respect the desired one. In this case, where the robots are in formation, all the individual homographies induced by pairs of robots are the same, and they are also equal to the homography computed from all the robots (10).

In the case in which the robots are not in the desired configuration, the relative motion of the robots between the current and target images is not rigid, which means that the homographies induced by each pair of robots are different. In this case, the computation of the homography from all the robots gives a matrix of the form:

$$\mathbf{H}_{nonrigid} = \begin{bmatrix} s \cos \theta & s \sin \theta & h_{13} \\ -s \sin \theta & s \cos \theta & h_{23} \\ 0 & 0 & 1 \end{bmatrix}, \quad (11)$$

where the upper left hand 2×2 matrix is no longer orthogonal for $s \neq 1$. This previous matrix corresponds to a similarity transformation, i.e. translation, rotation and isotropic scaling represented by the scalar s . This transformation preserves angles and ratios of lengths. The eigenvalues of this similarity are $\{1, s e^{i\theta}, s e^{-i\theta}\}$ and encapsulate the rotation angle. Comparison with the expression of the homography (7) yields to a non-coherent relative motion of the robots. Therefore, the nonrigid motion of the robots induces a homography which is valid but not constrained to the expected matrix form (7). It only remains to define a desired homography like $\mathbf{H}_{nonrigid}$, but being induced by a motion that keeps the homography and rigidity constraints. This can be done by normalizing the upper left hand 2×2 matrix of (11) to be orthogonal. Then, we obtain the desired homography as

$$\mathbf{H}^d = \mathbf{H}_{nonrigid} \begin{bmatrix} 1/s & 0 & 0 \\ 0 & 1/s & 0 \\ 0 & 0 & 1 \end{bmatrix}, \quad (12)$$

where s can be computed from $s^2 = \det(\mathbf{H}_{nonrigid})$. The goal is to control the robots in such a way that all the homographies are led to \mathbf{H}^d and therefore, the desired configuration is reached.

The homography $\mathbf{H}_{nonrigid}$ relates each point \mathbf{p} of the current image with the corresponding point \mathbf{p}' in the desired formation image with $\mathbf{p}' = \mathbf{H}_{nonrigid} \mathbf{p}$. The desired homography \mathbf{H}^d is used now to define the goal location of the robots/points in the image as $\mathbf{p}^d = (\mathbf{H}^d)^{-1} \mathbf{p}'$. Notice that the desired location of the robots in the image computed from the desired homography is not constant and varies with time, depending on the motion of the camera and the robots.

III. VISUAL CONTROL LAW

From the desired homography computed as explained in the previous section, we propose a control scheme to drive the robots to the desired configuration defined by an image of that configuration. An overview of the control loop is depicted in Fig. 2.

A. Robot Model and Coordinate Systems

Different coordinate systems defined in the 3D space are depicted in Fig. 3. The state \mathbf{x} of each robot is denoted as

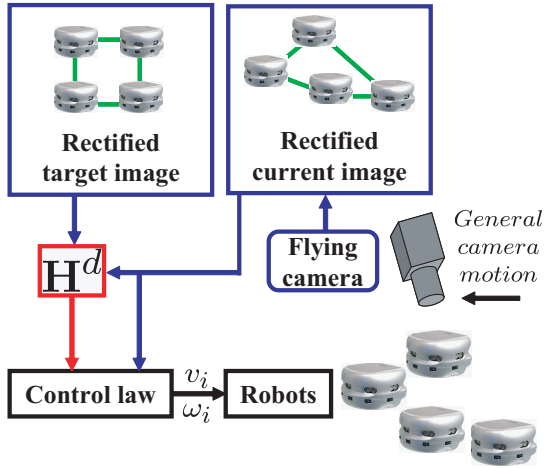


Fig. 2. Overview of the control loop. In each loop of the control, the flying camera takes a current image of the robots, the desired homography \mathbf{H}^d is computed from the rectified current-target correspondences and used in the control law to compute the robot velocities necessary to reach the desired configuration of the multi-robot system.

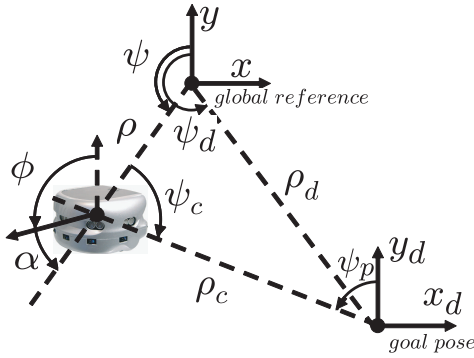


Fig. 3. Coordinate systems from a top view of the 3D scene.

$(x, y, \phi)^T \in \mathbb{R}^3$ in Cartesian coordinates or $(\rho, \alpha, \phi)^T \in \mathbb{R}^3$ in polar coordinates. The robots are steered with $(v, \omega)^T \in \mathbb{R}^2$, where the linear velocity v is in the direction of the robot y -axis and the angular velocity ω is around the robot z -axis. We describe the position and orientation of each robot in terms of the subgroup of planar motion $SE(2)$ of the Euclidean group in \mathbb{R}^3 . Expressing the kinematic equations of each robot in polar or Cartesian coordinates in a fixed reference gives

$$\begin{cases} \dot{\rho} = v \cos \alpha \\ \dot{\alpha} = -\omega + \frac{v}{\rho} \sin \alpha \\ \dot{\phi} = \omega \end{cases}, \text{ and } \begin{cases} \dot{x} = -v \sin \phi \\ \dot{y} = v \cos \phi \\ \dot{\phi} = \omega \end{cases}, \quad (13)$$

respectively, being

$$x = -\rho \sin \psi \quad \text{and} \quad y = \rho \cos \psi. \quad (14)$$

The alignment error α is defined as the angle between the robot body y -axis and the distance vector ρ ,

$$\alpha = \psi - \phi. \quad (15)$$

We now introduce several variables to define the state of each robot on the image plane with (ρ_m, ψ_m, ϕ_m) . These variables are depicted in Fig. 4. The origin of the coordinate

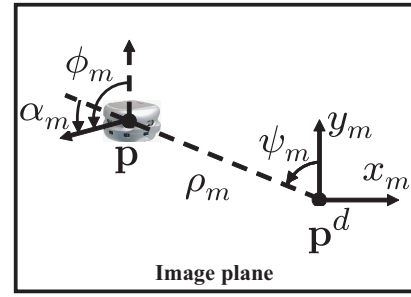


Fig. 4. Coordinate systems on the image plane for a robot. Subindex m denotes that the variable is defined on the image plane (the same variable without subindex m refers to the 3D space). Point \mathbf{p} is the image projection of a robot and \mathbf{p}^d its location to reach the desired configuration of the multi-robot system.

system for each robot \mathbf{p} on the image plane is placed in the desired location \mathbf{p}^d , i.e. the robots are in the desired configuration when all of them are in the origin of their respective references (\mathbf{p}^d).

The variable ρ_m is the distance of the projection of a robot in the image \mathbf{p} with respect to its desired position in the image \mathbf{p}^d , and so

$$\rho_m = \sqrt{(p_x - p_x^d)^2 + (p_y - p_y^d)^2}, \quad (16)$$

and

$$\psi_m = \text{atan2}(- (p_x - p_x^d), (p_y - p_y^d)), \quad (17)$$

where function atan2 returns the value of the arc tangent using the sign of the arguments to determine the quadrant. ϕ_m can be computed directly from the image of the robot or estimated with $\phi_m = \text{atan2}(-\Delta p_x, \Delta p_y)$. The alignment error on the image α_m is also defined as $\alpha_m = \phi_m - \psi_m$.

B. Control Law

The control law is defined as a sequence of two steps with their respective controllers for each robot. The goal of the first step is to drive the robots to their target positions in such a way that the robots are in the desired formation up to orientation, while the second step corrects the orientation of each robot within the formation. Note that the motion of each robot is not independent of the rest of the team; they are all related through the homography by the definition of the desired configuration.

In the first step, the rotational velocity is defined in such a way that the robots move toward their desired locations while the linear velocity is obtained as a function of the distance to the target in image coordinates. Then, the first controller is defined for the robot i , with $i = 1, \dots, N$, as

$$\text{Step 1 } \begin{cases} v^i = k_v \rho_m^i \\ \omega^i = k_\omega (\alpha_m^i - \pi) \end{cases}, \quad (18)$$

where $k_v > 0$ and $k_\omega > 0$ are control gains. The image projection of the distance to the desired position ρ_m^i and the value of the alignment error α_m^i are measured directly on the image plane.

After the first step, the robots are in formation and only a pure rotation is needed to reach the desired configuration of

the robot team. The controller for the second step is defined as

$$\text{Step 2} \begin{cases} v^i = 0 \\ \omega^i = -k_\omega ((\phi_m^i - \psi_{Fm}) - (\phi_m^{0i} - \psi_{Fm}^0)) \end{cases}, \quad (19)$$

where ψ_{Fm} is a representative angle of the robot formation and it is used to define the relative angles of the robots within the formation in the image plane. The parameter ψ_{Fm} is defined for any pair of robots (j, k) as

$$\psi_{Fm} = \text{atan2}(-(\rho_x^j - \rho_x^k), (\rho_y^j - \rho_y^k)). \quad (20)$$

The values of j and k are selected arbitrarily (with $j, k \in \{1..N\}$ and $j \neq k$) to be used in (19). The superindex 0 in ϕ_m^0 or ψ_{Fm}^0 refers to the values of the variables in the reference image.

C. Stability Analysis

In this section, the stability of the control scheme is analyzed by means of *Lyapunov's Direct Method*.

Proposition 3.1: The closed-loop system (13) is asymptotically stable under the control scheme (18)-(19).

Proof: The control scheme consists of two sequential controllers that are analyzed step by step in the following.

1) *Step 1:* The robots perform a motion under the control law (18), and we define the Lyapunov candidate function as

$$V_1^G = V_\rho^G + V_\alpha^G = \sum_{i=1}^N V_1^i = \sum_{i=1}^N (V_\rho^i + V_\alpha^i), \quad (21)$$

being N the number of robots. The following analysis is referred to any robot i , and once V_1^i is proved to be Lyapunov, it trivially follows that the candidate function (21) is also Lyapunov. Hereafter, we omit the superindex i for ease of notation. The corresponding terms of (21) are defined as

$$V_\rho = (\rho_c)^2/2, \quad (22)$$

$$V_\alpha = (\alpha - \psi_c - \pi)^2/2. \quad (23)$$

The function V_1 is positive definite, given that $V_1(\mathbf{x}) > 0$ for all $\mathbf{x} \neq \mathbf{0}$ and $V_1(\mathbf{0}) = 0$. The derivative of the term V_α is given as

$$\dot{V}_\alpha = (\alpha - \psi_c - \pi) \left(-\omega + \frac{v}{\rho_c} \sin(\alpha - \psi_c) \right) + A, \quad (24)$$

where the term A represents the influence on \dot{V}_α of the variation of the robot goal location because of the combined motion of the set of robots through the homography:

$$\begin{aligned} A &= (\alpha - \psi_c - \pi) \cdot \dot{\psi}_c = (\alpha - \psi_c - \pi) \\ &\cdot (\dot{\rho}\rho_d \sin(\psi - \psi_d) (\rho_c^2 - \rho^2 - \rho_d^2) \\ &+ \rho\dot{\rho}_d \sin(\psi - \psi_d) (\rho_c^2 + \rho^2 + \rho_d^2) \\ &+ \rho\rho_d(\dot{\psi} - \dot{\psi}_d) \cos(\psi - \psi_d) (\rho_c^2 + \rho^2 + \rho_d^2) \\ &+ 2\rho\rho_d\rho_c\dot{\rho}_c \sin(\psi - \psi_d) / (2\rho^2\rho_c^2), \end{aligned} \quad (25)$$

where ρ_d , x_d , y_d and ψ_p are defined for one robot in Fig. 3, and the corresponding derivatives are given as follows:

$$\begin{aligned} \dot{\rho} &= v \cos \alpha, \\ \dot{\psi} &= (v \sin \alpha) / \rho, \\ \dot{\rho}_c &= v \cos(\alpha - \psi_c) + \dot{x}_d \sin \psi_p + \dot{y}_d \cos \psi_p, \\ \dot{\rho}_d &= (x_d \dot{x}_d - y_d \dot{y}_d) / \rho_d, \\ \dot{\psi}_d &= (x_d \dot{\rho}_d - \dot{x}_d \rho_d) / (\cos \psi_d \rho_d^2). \end{aligned} \quad (26)$$

Developing the expression of \dot{V}_α with the values of v and ω , we obtain

$$\begin{aligned} \dot{V}_\alpha &= -k_\omega (\alpha - \psi_c - \pi) (\alpha_m - \pi) + A \\ &+ k_v \frac{\rho_m}{\rho_c} (\alpha - \psi_c - \pi) \sin(\alpha - \psi_c) \\ &= -k_\omega (\alpha - \psi_c - \pi) (\alpha_m - \pi) + A \\ &- k_v \frac{\rho_m}{\rho_c} (\alpha - \psi_c - \pi) \sin(\alpha - \psi_c - \pi). \end{aligned} \quad (27)$$

Notice that α_m is the image projection of $(\alpha - \psi_c)$ and therefore $\text{sign}(\alpha - \psi_c - \pi) = \text{sign}(\alpha_m - \pi)$. Then, all the terms of \dot{V}_α are negative except A , which can be positive or negative and is analyzed later.

In addition, the derivative of V_ρ is given as

$$\begin{aligned} \dot{V}_\rho &= \rho_c \dot{\rho}_c = \rho_c v \cos(\alpha - \psi_c) + R \\ &= k_v \rho_c \rho_m \cos(\alpha - \psi_c) + R, \end{aligned} \quad (28)$$

where the term R represents the influence on \dot{V}_ρ of the variation of the robot goal location because of the combined motion of the set of robots through the homography:

$$R = \rho_c (\dot{x}_d \sin \psi_p + \dot{y}_d \cos \psi_p). \quad (29)$$

The previous derivative (28) can be positive or negative depending on the value of $(\alpha - \psi_c)$ and R , which is analyzed later. There are two possible cases: The first term of (28) is negative if $|\alpha - \psi_c| > \pi/2$ or positive if $|\alpha - \psi_c| \leq \pi/2$. This second case requires further analysis. Thus, we now study the conditions that make $\dot{V}_1 < 0$ when $|\alpha - \psi_c| \leq \pi/2$. We can write the following expressions:

$$\begin{aligned} \dot{V}_1 &= \dot{V}_\alpha + \dot{V}_\rho \\ \dot{V}_1 &= -k_\omega (\alpha - \psi_c - \pi) (\alpha_m - \pi) \\ &- k_v \frac{\rho_m}{\rho_c} (\alpha - \psi_c - \pi) \sin(\alpha - \psi_c - \pi) \\ &+ k_v \rho_c \rho_m \cos(\alpha - \psi_c) + Q \\ \dot{V}_1 &< -k_\omega (\alpha - \psi_c - \pi) (\alpha_m - \pi) \\ &+ k_v \rho_c \rho_m \cos(\alpha - \psi_c) + Q, \end{aligned} \quad (30)$$

where we denote $Q = A + R$. In the considered case ($|\alpha - \psi_c| \leq \pi/2$), we can determine the upper and lower bounds of the terms in (30). On the one hand, the worst case for the first term of \dot{V}_α is when $(\alpha - \psi_c - \pi) = -\pi/2$, i.e. $(\alpha - \psi_c) = \pi/2$ and $\alpha_m = \pi/2$. On the other hand, the worst case for \dot{V}_ρ is when $|\alpha - \psi_c| = 0$. Then,

$$\dot{V}_1 < -k_\omega (\pi^2/4) + k_v \rho_c \rho_m + Q. \quad (31)$$

The condition for $\dot{V}_1 < 0$ can be derived from the last equation as

$$k_\omega > \frac{4}{\pi^2} (k_v \rho_c \rho_m + Q). \quad (32)$$

Notice that the values of ρ_c and ρ_m are finite in a real application and lead to an upper bound (i.e. we assume that the robots are not placed initially at infinite distance). Notice also that the terms A (25) and R (29) in Q are smooth and bounded functions assuming again that the robots are initially placed at finite distance. Additional development is necessary to show that terms \dot{x}_d and \dot{y}_d in Q are bounded. For each robot, the vector $\mathbf{x}_d = (x_d, y_d, z_d, 1)$ in homogeneous coordinates is the reprojection of the desired image point position of the robot $\mathbf{p}^d = (p_x^d, p_y^d, 1)$ to the 3D space. The point projection is given by $\mathbf{p}^d = \mathbf{K} \mathbf{P} \mathbf{x}_d$ where $\mathbf{K} \in \mathbb{R}^{3 \times 3}$ is the camera calibration matrix and $\mathbf{P} \in \mathbb{R}^{3 \times 4}$ is the projection matrix [24]. Additionally, we defined in Section II-D that $\mathbf{p}^d = (\mathbf{H}^d)^{-1} \mathbf{p}'$, being \mathbf{p}' the point coordinates on the target image. Thus, we can write

$$\mathbf{x}_d = \mathbf{P}^+ \mathbf{K}^{-1} (\mathbf{H}^d)^{-1} \mathbf{p}', \quad (33)$$

being \mathbf{P}^+ the pseudo-inverse of \mathbf{P} . Given that \mathbf{K} and \mathbf{p}' are constant, the derivative of the previous expression yields

$$\dot{\mathbf{x}}_d = \left(\dot{\mathbf{P}}^+ \mathbf{K}^{-1} (\mathbf{H}^d)^{-1} + \mathbf{P}^+ \mathbf{K}^{-1} (\dot{\mathbf{H}}^d)^{-1} \right) \mathbf{p}'. \quad (34)$$

The derivative of the projection camera matrix \mathbf{P} is bounded given that it depends on the arbitrary camera motion, which is assumed to be bounded. The derivative of the desired homography \mathbf{H}^d is also bounded as it depends on the bounded camera motion and the motion of the robots, which are assumed to be initially placed at a finite distance. Then, the values \dot{x}_d and \dot{y}_d are bounded. We also need to check possible singularities that could make Q unbounded. In particular, there would be singularities when the following terms are equal to zero: ρ , ρ_c , ρ_d , and $\cos \psi_d$. On the one hand, given that the global coordinate system can be chosen arbitrarily, without loss of generality we can select this reference guaranteeing that $\rho \neq 0$, $\rho_d \neq 0$, and $\cos \psi_d \neq 0$. On the other hand, we have ρ_c equal to zero when the desired formation is reached. In that case, $\rho_c = 0$ implies $\rho = \rho_d$, $\psi = \psi_d$ and $\mathbf{H} = \mathbf{H}^d$, which also implies that $v = 0$, $\dot{x}_d = 0$ and $\dot{y}_d = 0$, finally yielding the bounded value $Q = 0$.

Therefore, suitable values can be found to define the control gains k_v and k_ω so that condition (32) holds. Under this condition, which in fact is rather conservative, $\dot{V}_1 < 0$ is guaranteed. Therefore, the control in the first step is asymptotically stable.

We can also approximate the time response of this first step by considering that the motion of the goal formation in the image is not significant in comparison with the robots' motion ($Q \approx 0$) and that the rotational correction is faster than the distance correction ($\alpha - \psi_c \approx \pi$). The validity of both approximations were supported by the experimental evaluation. We also denote k_ρ as the constant ratio ρ_m / ρ_c which depends on the camera calibration parameters and the image rectification procedure. Then, from (21) and (30) and using the above mentioned approximations, we can write: $\dot{V}_1 \approx -2k_v k_\rho V_1$. The solution of this first-order equation is $V_1(\mathbf{x}, t) \approx V_1(\mathbf{x}, 0) \exp(-2k_v k_\rho t)$. This approximation presents an exponential convergence rate $2k_v k_\rho$ of the first step controller that can be tuned with the value of k_v .

2) *Step 2*: The robots perform a pure rotation such that the desired relative orientation of the robots in the formation is achieved. The Lyapunov function is defined as

$$V_2^G = \sum_{i=1}^N V_2^i, \quad (35)$$

where the robot i gives

$$V_2^i = (\phi^i - \psi_F - \phi^{0i} + \psi_F^0)^2 / 2, \quad (36)$$

where the parameter ψ_F is defined similarly to (20) for any pair of robots ($j, k \in \{1..N\}$ with $j \neq k$) in the 3D space as

$$\psi_F = \text{atan2}(-(x^j - x^k), (y^j - y^k)). \quad (37)$$

The superindex 0 in ϕ^0 or ψ_F^0 refers to their corresponding values in the desired formation of the reference image. Given that the input information is defined by a similarity transformation, which preserves angles and ratios of lengths, we have that the projection of ψ_F is equal to ψ_{Fm} (and equivalently, the projection of ψ_F^0 to ψ_{Fm}^0).

In the following, we omit the superindex i for ease of notation. The function V_2 is positive definite given that $V_2(\mathbf{x}) > 0$ for all $\mathbf{x} \neq \mathbf{0}$ and $V_2(\mathbf{0}) = 0$. The derivative of V_2 yields

$$\begin{aligned} \dot{V}_2 &= (\phi - \psi_F - \phi^0 + \psi_F^0) \omega \\ &= -k_\omega (\phi - \psi_F - \phi^0 + \psi_F^0) (\phi_m - \psi_{Fm} \\ &\quad - \phi_m^0 + \psi_{Fm}^0). \end{aligned} \quad (38)$$

It can be seen that both multiplying terms of \dot{V}_2 correspond to the rotational error with the same sign. Therefore, \dot{V}_2 is negative definite and the control in the second step is asymptotically stable. Moreover, from (38) we can write $\dot{V}_2 = -2k_\omega V_2$. The solution of this first-order equation is $V_2(\mathbf{x}, t) = V_2(\mathbf{x}, 0) \exp(-2k_\omega t)$. This guarantees the exponential convergence of V_2 to zero, and the exponential convergence rate of the state can be determined by $2k_\omega$.

We have analyzed the stability in each of the two sequential steps showing that the individual controllers are asymptotically stable. In our control scheme, the switching of the control laws is performed ensuring that the system under the first controller will switch, in finite time, to the second controller when the error is lower than a threshold. Therefore, we can conclude that the system is asymptotically stable under the control scheme (18)-(19). ■

IV. EXPERIMENTS

In this section, simulations and real experiments showing the performance of the control scheme are presented.

A. Simulations

The virtual environment of the simulations assumes that the projection of the robots in the images can be detected and identified in order to match each robot with its correspondence in the other images. The results of two experiments are shown in Figs. 5 and 6.

In the first example, four robots are considered while the flying camera motion follows a helix with variable radius. The robots are initially in an arbitrary configuration and the goal

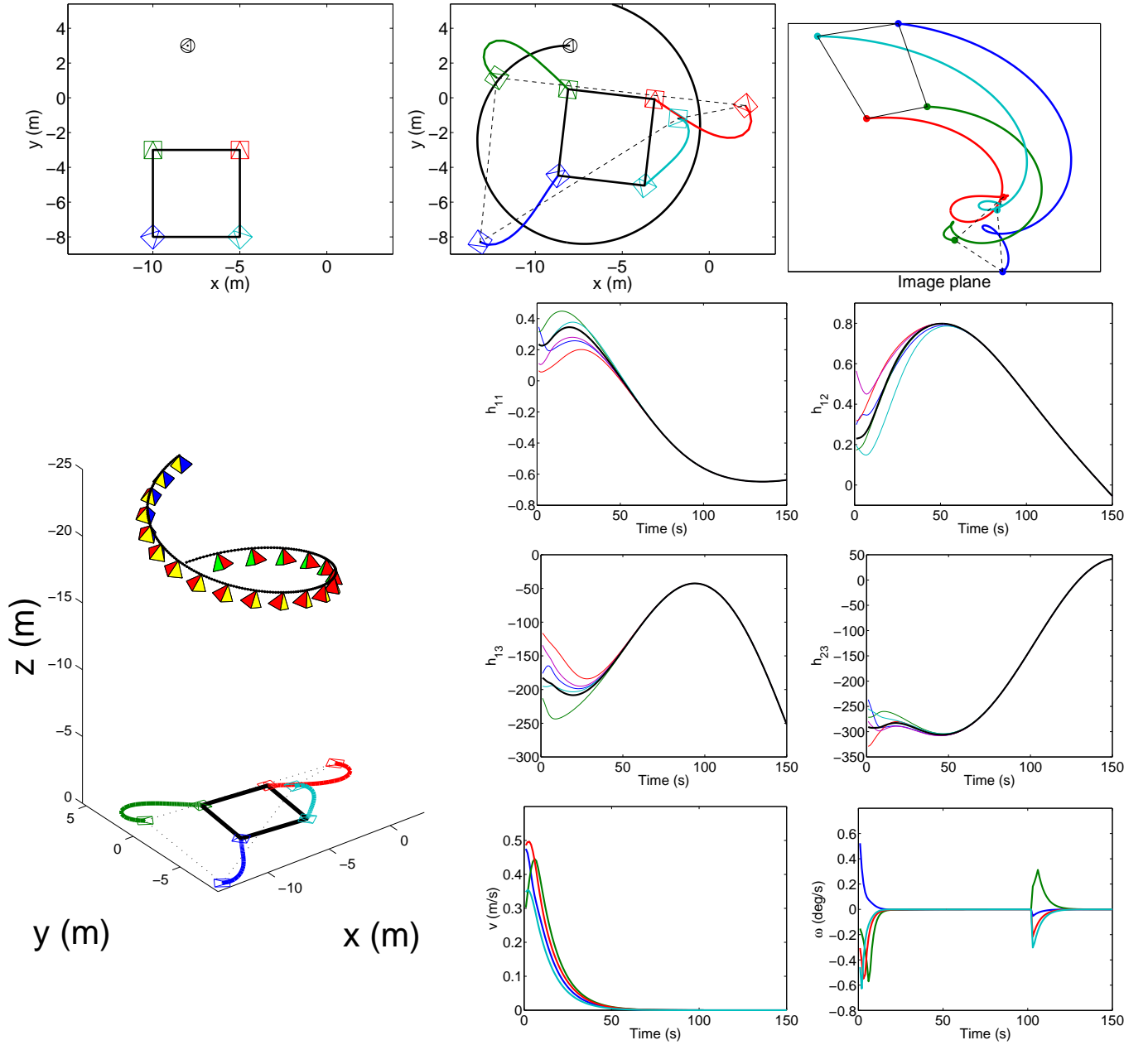


Fig. 5. Simulation with the flying camera undergoing a motion following a helix with variable radius. Top-left: Desired configuration for 4 robots in a square. Top-middle: Top view of the camera (the initial position of the camera is depicted with a triangle inside a circle) and the robots. The initial configuration is drawn with dashed line and the path followed by the robots to reach the desired configuration is shown (thick lines). Top-right: Trace of the robots in the image plane. Second row: 3D view of the camera and robots motion. Evolution of entries (h_{11} , h_{12} , h_{13} , h_{23}) of the desired (thick lines) and current (thin lines) homographies between the robots. Linear and angular velocities of the robots.

is to reach the desired one which, in this case, is a square. Figure 5 shows the desired configuration of the robots and their motion from their initial positions to the final ones. It can be seen that the desired configuration is correctly reached both in shape and size. The trace of the robots projected in the image plane is also depicted. The behavior of the points in the image is not intuitive because it is the result of the combined motion of the robots and the camera. The plots of the evolution of the homography entries show that they converge to the desired values of the homographies. Only entries h_{11} , h_{12} , h_{13} , and h_{23} are depicted given that $h_{22} = h_{11}$ and $h_{21} = -h_{12}$. Thus, the robots reach the

desired formation when the common homography is finally obtained. Notice that the final homography does not converge to a constant value given that it evolves because of the arbitrary motion of the camera.

In the second example (Fig. 6), six robots are considered while the flying camera follows a circular motion compounded with sinusoids in the vertical direction. In this case, the desired formation is a triangle. Similarly to the previous example, the motion of the camera and the robots as well as the evolution of different variables are depicted. As can be seen, the homography entries converge to the desired ones and the robots reach the desired configuration independently of the

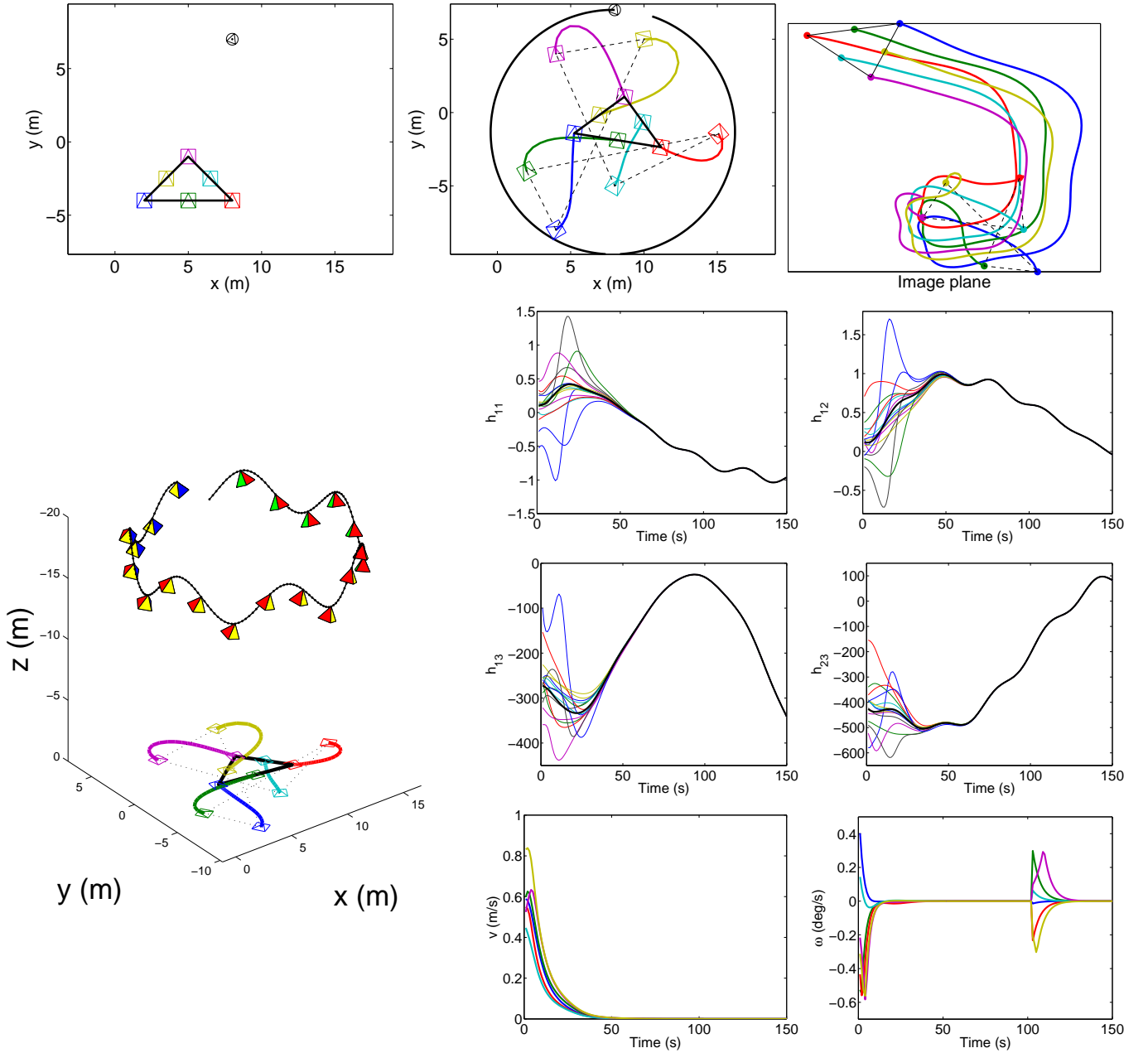


Fig. 6. Simulation with the flying camera undergoing a circular motion compounded with sinusoids in the vertical direction. Top-left: Desired configuration for 6 robots in a triangle. Top-middle: Top view of the camera (the initial position of the camera is depicted with a triangle inside a circle) and the robots. The initial configuration is drawn with dashed line and the path followed by the robots to reach the desired configuration is shown (thick lines). Top-right: Trace of the robots in the image plane. Second row: 3D view of the camera and robots motion. Evolution of entries (h_{11} , h_{12} , h_{13} , h_{23}) of the desired (thick lines) and current (thin lines) homographies between the robots. Linear and angular velocities of the robots.

arbitrary camera motion. Additional simulations depicting the motion of the robots and the camera are shown in the video attachment (**Video 1**).

From a practical point of view, we have to consider the effect of disturbances or noise in the control loop to evaluate its behaviour in that situation. Thus, the next simulations evaluate the performance of the control scheme in the presence of image noise. For this purpose, Gaussian image noise is added to the image information used in the control loop. The results of Fig. 7 correspond to an experiment that has been carried out using the same setup of the simulation in Fig. 5, but in the presence of image noise with standard deviation $\sigma = 3$

pixels. The evolution of the system and different variables are depicted in Fig. 7. It can be seen that the noisy measurements are directly propagated from the image plane to the computed homographies, and also to the desired target homography, and finally to the computed velocities for the robots. Despite the noisy input information, the system behaves correctly showing robust performance. The result of another test is also provided in the bottom-left graph of Fig. 7. In this test, the control is executed with different levels of image noise. In particular, Gaussian image noise is added to the image information with standard deviation σ from 0 to 10 pixels. For each execution, the distances between the robots in the obtained final formation

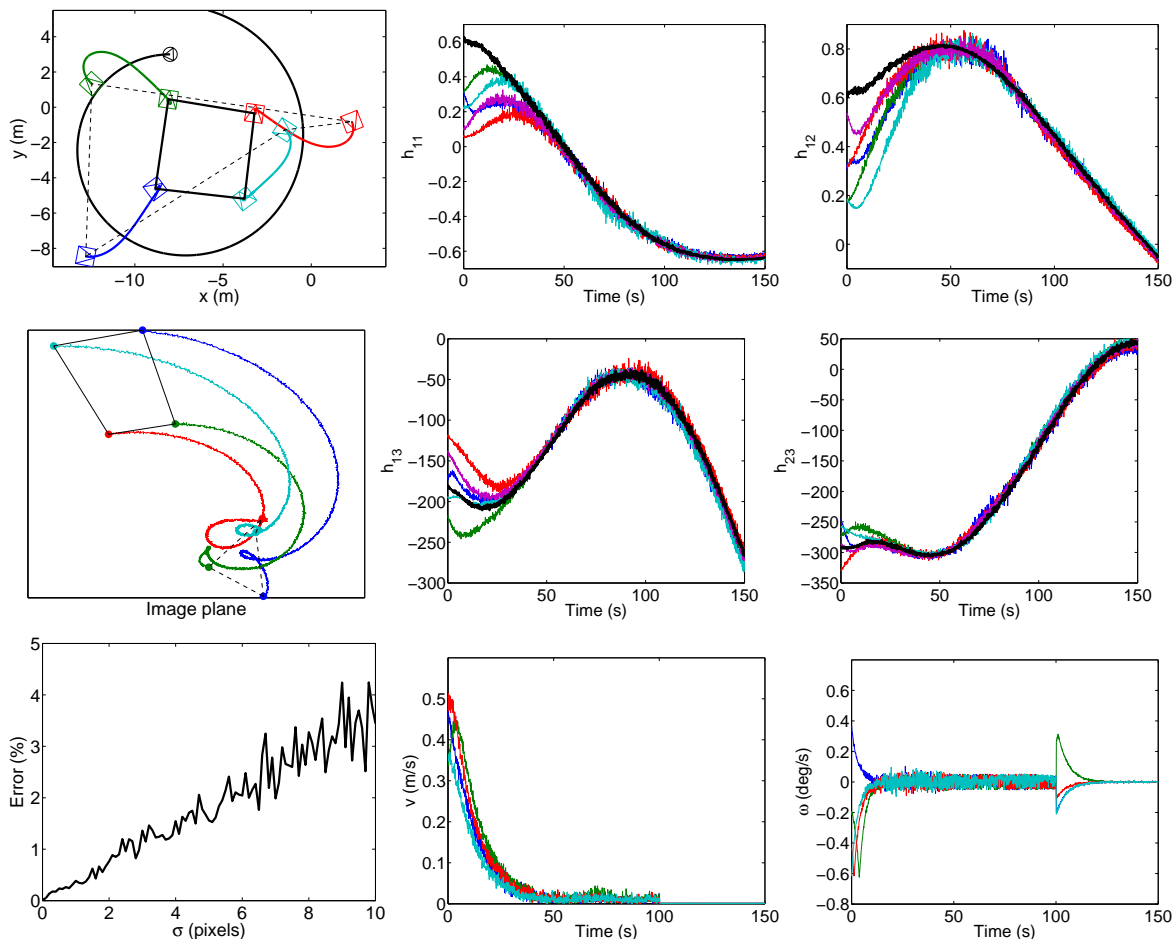


Fig. 7. Simulation of Fig. 5 in the presence of image noise with $\sigma = 3$ pixels. Top-left: Top view of the camera (the initial position of the camera is depicted with a triangle inside a circle) and the robots. Middle-left: Trace of the robots in the image plane. Top-right: Evolution of entries (h_{11} , h_{12} , h_{13} , h_{23}) of the desired (thick lines) and current (thin lines) homographies between the robots. Bottom-right: Linear and angular velocities of the robots. Bottom-left: distance error in the final formation for a set of experiments with different values of image noise from σ of 0 to 10 pixels.

are compared with the desired formation and depicted in percentage. The corresponding plot provided in Fig. 7 shows that the obtained error increases in an approximately linear trend with the image error. This result demonstrates that the controlled system performs properly in the presence of the different levels of noise.

The control scheme was also tested against variation of the camera calibration parameters. In particular, the focal length of the camera is modified during the control simulating the use of the zoom. The same setup of the first simulation (Fig. 5) is used again but changing the focal length from 12 mm at the beginning of the simulation to 6 mm at the end. The result of this experiment is depicted in Fig. 8, where the motion of the camera and the robots as well as the evolution of different variables are depicted. As expected, the images obtained compared with the first simulation are different as they depend on the intrinsic camera parameters, and this is confirmed checking the trace of the robots on the image plane depicted in Fig. 8. Consequently the obtained values of the homography entries are also different. However, the desired square configuration is reached correctly independently of the focal length variations without affecting the control performance.

From the point of view of the local navigation, one issue

when dealing with multi-robot systems is the problem of obstacle avoidance. This issue is out of the scope of this work and the procedures presented in [5], [29], [30] could be used here.

B. Real Experiments

The real experiments were carried out with the robot platforms shown in Fig. 9. The size of the robots is 13 cm of diameter and 7 cm of height. The uncalibrated external camera is connected through Firewire to a laptop, an Intel® Core™ 2 Duo CPU at 2.50 GHz with operating system Ubuntu Linux. Different camera lenses have been used in the results provided, in particular with a focal length of 3 mm, or 4.8 mm. The robots are equipped on top with patterns consisting of circular codes that allow their detection and identification in the images. The images are acquired with size 1280×960 pixels and the image processing relays on the OpenCV library. The robot velocities computed using the control scheme presented are sent to the robots by Wireless Ethernet network communication. Currently, the control loop of the implementation runs at 8 frames per second.

An example of the rectifying procedure presented in Section II-B is given in Fig. 10. This image has been acquired with a

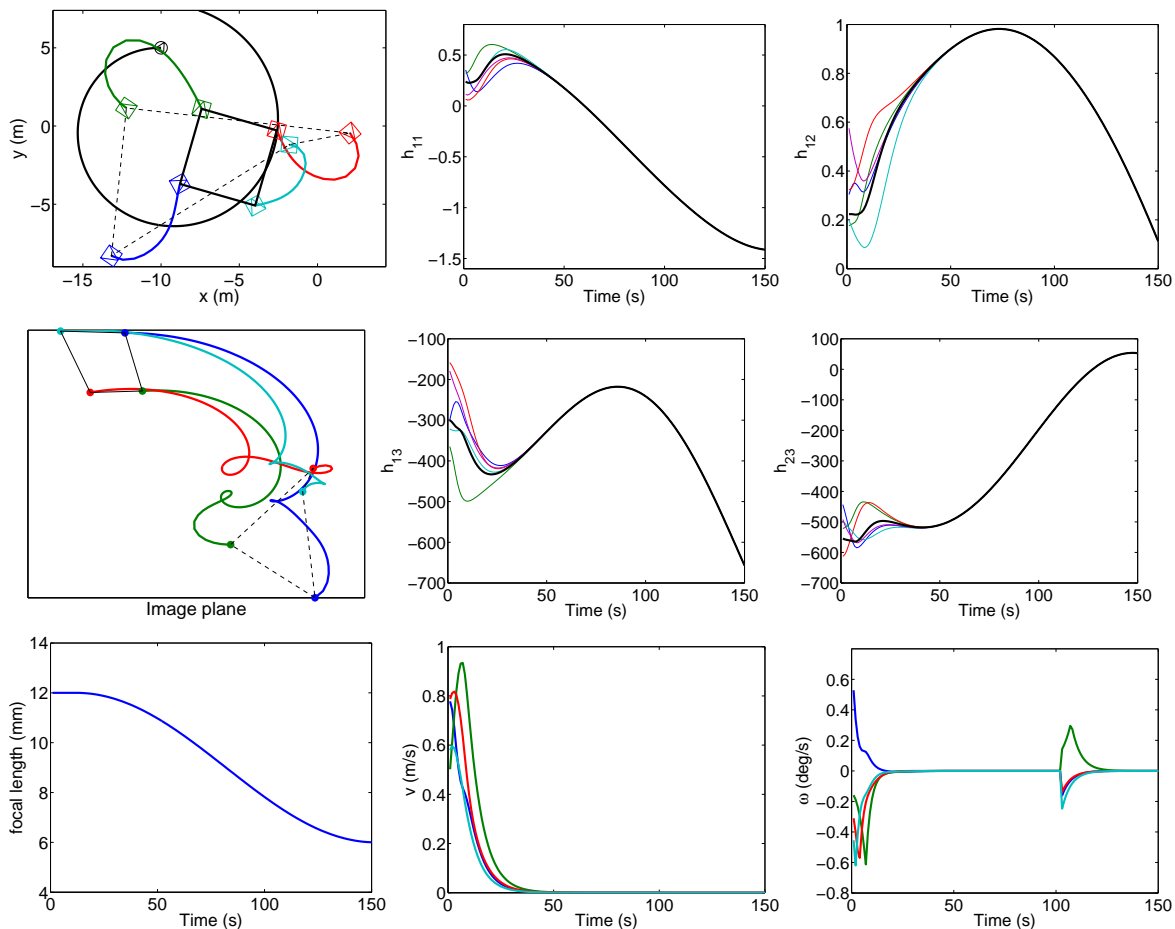


Fig. 8. Simulation of Fig. 5 with arbitrary modification of camera calibration parameters. Top-left: Top view of the camera (the initial position of the camera is depicted with a triangle inside a circle) and the robots. Middle-left: Trace of the robots in the image plane. Bottom-left: arbitrary focal length variation during the experiment. Top-right: Evolution of entries (h_{11} , h_{12} , h_{13} , h_{23}) of the desired (thick lines) and current (thin lines) homographies between the robots. Bottom-right: Linear and angular velocities of the robots.

Canon Digital IXUS 800 camera. The robots are in the desired configuration, a square, and they are labelled with circular codes used for their detection and identification. Four circular codes are also set on the corners of the workspace for carrying out the rectification processing in a simple way. Because of the projective transformation through the camera imaging, the square formation is seen as a rhombus on the image plane and, after the rectification, the obtained image shows that the multi-robot formation in the image corresponds to an actual square. Notice that the image is rectified to a similarity transformation, and no metric information is required for this process. In particular, the parallel and orthogonal condition between the corners of the workspace is used. In the figure, all the image is rectified, whereas in the real experiments, only the points representing the robots are rectified.

The results of the first experiment are shown in Fig. 11. In this experiment, the external camera is fixed during the control. The camera mounts a lens with focal length of 3 mm. The target image is the one depicted in Fig. 10, where the desired configuration of the robots is a square. Initially, the robots are placed arbitrarily in the workspace. The path followed by each robot during the execution is plotted on the acquired final image. The results show that the control performs well and the



Fig. 9. Khepera III robot from K-Team S.A.

desired configuration is reached. For security and to prolong the battery duration, the maximum velocity of the robots is restricted to 3 cm/s as can be seen in the plot of the linear velocities.

The next experiment employs the same previous target image and is carried out following an arbitrary camera motion using a hand held camera mounting a lens of focal length 4.8 mm. Sequences of images acquired in two different experiments are displayed in Fig. 12. The first image corresponds to the robots in the initial arbitrary configuration, two intermediate images are shown and the last image depicts the robots at the end of the experiment, showing convergence to the desired configuration. The motion of the robots in one experiment tracked in the image plane is depicted in Fig. 13. It can be seen

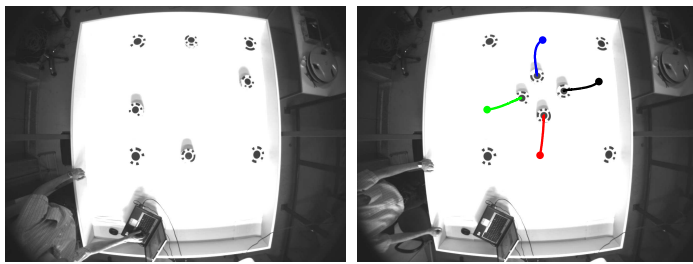


Fig. 11. Results of a real experiment. From left to right: Initial image; Final image where the robots have reached the desired squared configuration (The tracks of the robots during their motion are drawn); Right: Linear and angular velocities sent to the robots, respectively.

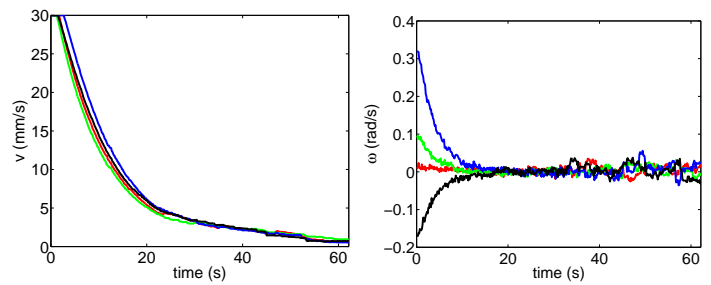


Fig. 10. Left: Reference image of the desired multi-robot configuration. Right: target image after rectification.

that the trajectories of the robots in the image plane are quite contorted because of the arbitrary motion of the camera and the unsteady hand of the camera carrier. The velocities computed by the control scheme and sent to the robots are also depicted in Fig. 13. The results show that the control scheme deals properly with the arbitrary motion of the camera leading the robots to the desired configuration. Notice that, although the camera used during the experiment was different to the camera used to acquire the reference image, the performance of the approach is not affected and the system converges properly despite changes in the intrinsic camera parameters. The video attachment **Video 2** shows results from real experiments.

In some multi-robot applications, robots are required not only to achieve formations to accomplish complex tasks but also to move in formation. In this case, it is interesting for the multiple mobile robots to have the ability to move in formation along specified paths or to maintain the desired relationship of leader-follower formations. In fact, this is a natural extension of the work presented here. Although this application was not in the core of our proposal and it has not been developed, the method proposed can be used for following in formation a specified path or for following one robot as leader in formation. The simulation in **Video 3** is given as a mere example to illustrate this application. In this example, the group of robots moves in formation while following the leader, whose motion is unknown for the rest of the robots.

V. CONCLUSION

A new control scheme has been proposed to lead a group of robots to a desired configuration. The control law is based on

a particular homography parametrization that allows to define the desired location of the robots in the image plane. The advantages of this approach are the simplicity of the definition of any arbitrary desired configuration for the set of robots and that the control law does not require the knowledge of the arbitrary 3D motion of the uncalibrated flying camera. The validity of the approach is supported by simulations and real experiments that show the effectiveness and good performance of the homography-based control scheme. The application to multi-robot systems of the geometry-based approach proposed here through the homography is quite promising from the point of view of efficiency since all the required information in the control loop is encapsulated in just one homography. In particular, in each control loop only a linear system needs to be solved to compute the homography induced by the robots, which is a good property from the viewpoint of algorithm scalability.

ACKNOWLEDGMENT

The authors would like to thank A. Benzerrouk and L. Lequievre for their assistance in the experimental evaluation.

REFERENCES

- [1] J. Marshall, M. Broucke, and B. Francis, "Formations of vehicles in cyclic pursuit," *IEEE Transactions on Automatic Control*, vol. 49, no. 11, pp. 1963–1974, Nov. 2004.
- [2] W. Dong, "Flocking of multiple mobile robots based on backstepping," *IEEE Transactions on Systems, Man, and Cybernetics, Part B: Cybernetics*, vol. 41, no. 2, pp. 414–424, Apr. 2011.
- [3] J. Ghommam, H. Mehrjerdi, M. Saad, and F. Mnif, "Formation path following control of unicycle-type mobile robots," *Robotics and Autonomous Systems*, vol. 58, no. 5, pp. 727–736, 2010.
- [4] J. Chen, D. Sun, J. Yang, and H. Chen, "Leader-Follower Formation Control of Multiple Non-holonomic Mobile Robots Incorporating a Receding-horizon Scheme," *The International Journal of Robotics Research*, vol. 29, no. 6, pp. 727–747, 2010.
- [5] K. Listmann, M. Masalawala, and J. Adamy, "Consensus for formation control of nonholonomic mobile robots," in *IEEE International Conference on Robotics and Automation*, May 2009, pp. 3886–3891.
- [6] B. S. Park, J. B. Park, and Y. H. Choi, "Adaptive formation control of electrically driven nonholonomic mobile robots with limited information," *IEEE Transactions on Systems, Man, and Cybernetics, Part B: Cybernetics*, vol. 41, no. 4, pp. 1061–1075, Aug. 2011.
- [7] A. K. Das, R. Fierro, V. Kumar, J. P. Ostrowski, J. Spletzer, and C. J. Taylor, "A vision-based formation control framework," *IEEE Transactions on Robotics and Automation*, vol. 18, no. 5, pp. 813–825, 2002.
- [8] P. Yang, R. Freeman, and K. Lynch, "Multi-agent coordination by decentralized estimation and control," *IEEE Transactions on Automatic Control*, vol. 53, no. 11, pp. 2480–2496, Dec. 2008.

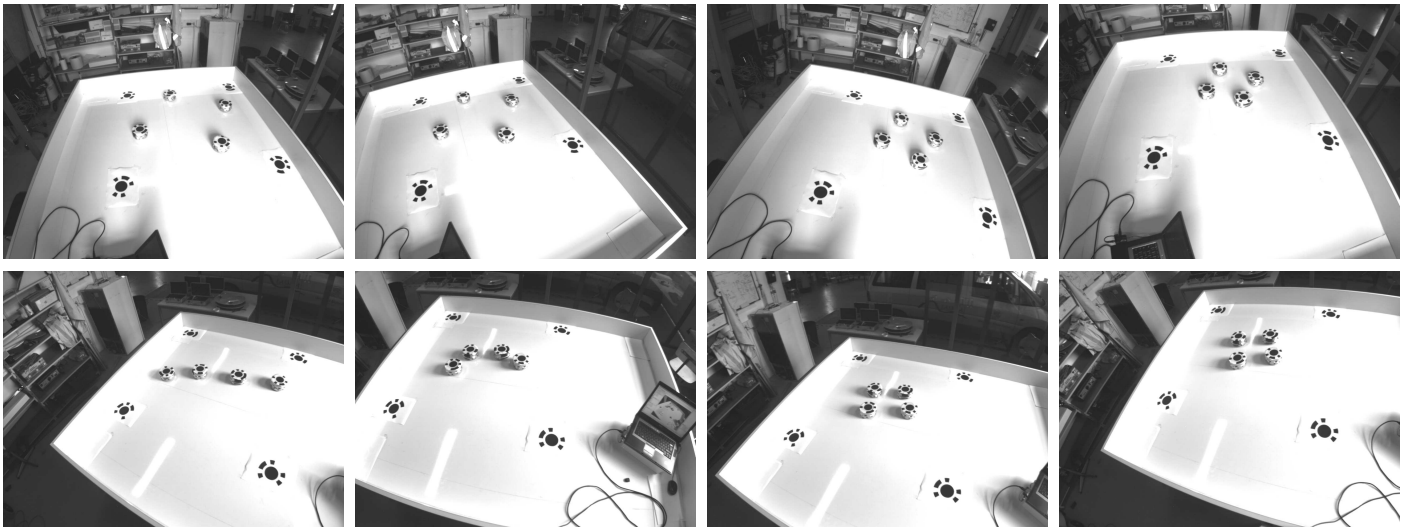


Fig. 12. Sequences of images acquired in two different experiments using a hand held camera following an arbitrary motion (first and second row, respectively). The left image is the initial one and the right image is the final one. Two intermediate images are shown in both cases.

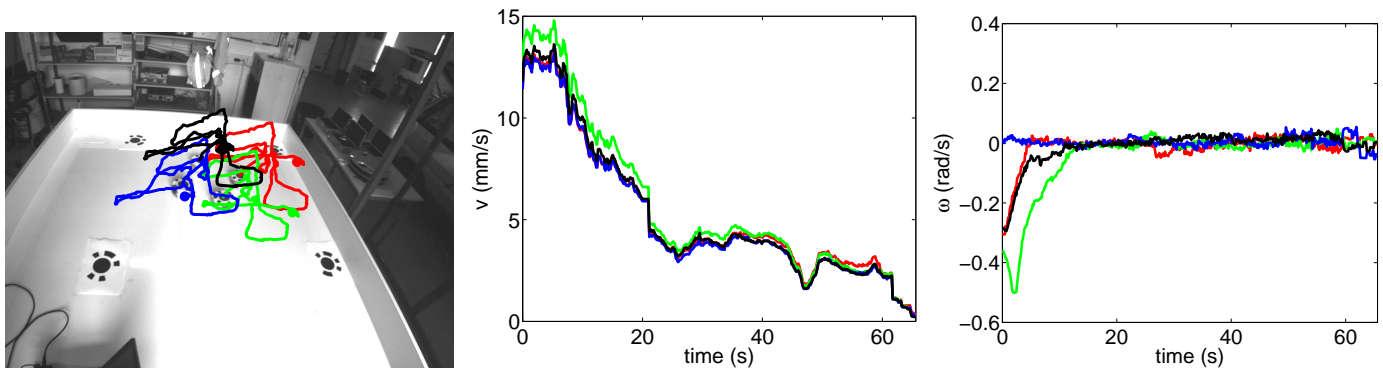


Fig. 13. Experiment using a hand held camera following an arbitrary motion. Left: evolution of the robots in the image plane, drawn on the final image. Right: linear and angular velocities sent to the robots, respectively.

- [9] N. Moshtagh, N. Michael, A. Jadbabaie, and K. Daniilidis, "Vision-based, distributed control laws for motion coordination of nonholonomic robots," *IEEE Transactions on Robotics*, vol. 25, no. 4, pp. 851–860, Aug. 2009.
- [10] J. Alonso-Mora, A. Breitenmoser, M. Rufli, R. Siegwart, and P. Beardsley, "Multi-robot system for artistic pattern formation," in *IEEE International Conference on Robotics and Automation*, May 2011, pp. 4512–4517.
- [11] S. Y. Chen, "Kalman filter for robot vision: a survey," *IEEE Transactions on Industrial Electronics*, 2012, 10.1109/TIE.2011.2162714.
- [12] F. Chaumette and S. Hutchinson, "Visual servo control, part I: Basic approaches," *IEEE Robotics and Automation Magazine*, vol. 13, no. 4, pp. 82–90, Dec. 2006.
- [13] S. Chen, Y. Li, and N. M. Kwok, "Active vision in robotic systems: A survey of recent developments," *The International Journal of Robotics Research*, vol. 30, no. 11, pp. 1343–1377, 2011.
- [14] H. Chen, D. Sun, and J. Yang, "Global localization of multirobot formations using ceiling vision SLAM strategy," *Mechatronics*, vol. 19, no. 5, pp. 617 – 628, 2009.
- [15] R. Vidal, O. Shakernia, and S. Sastry, "Following the flock: Distributed formation control with omnidirectional vision-based motion segmentation and visual servoing," *Robotics and Autonomous Magazine*, vol. 11, no. 4, pp. 14–20, 2004.
- [16] G. López-Nicolás, J. J. Guerrero, and C. Sagüés, "Visual control of vehicles using two-view geometry," *Mechatronics*, vol. 20, no. 2, pp. 315–325, 2010.
- [17] Y. K. Yu, K. H. Wong, M. M. Y. Chang, and S. H. Or, "Recursive camera-motion estimation with the trifocal tensor," *IEEE Transactions on Systems, Man, and Cybernetics, Part B: Cybernetics*, vol. 36, no. 5, pp. 1081–1090, Oct. 2006.
- [18] G. Blanc, Y. Mezouar, and P. Martinet, "Indoor navigation of a wheeled mobile robot along visual routes," in *IEEE International Conference on Robotics and Automation*, Apr. 2005, pp. 3365–3370.
- [19] Y. Fang, W. E. Dixon, D. M. Dawson, and P. Chawda, "Homography-based visual servo regulation of mobile robots," *IEEE Transactions on Systems, Man, and Cybernetics, Part B: Cybernetics*, vol. 35, no. 5, pp. 1041–1050, 2005.
- [20] J. Courbon, Y. Mezouar, and P. Martinet, "Indoor navigation of a non-holonomic mobile robot using a visual memory," *Autonomous Robots*, vol. 25, no. 3, pp. 253–266, 2008.
- [21] G. López-Nicolás, N. R. Gans, S. Bhattacharya, J. J. Guerrero, C. Sagüés, and S. Hutchinson, "Homography-based control scheme for mobile robots with nonholonomic and field-of-view constraints," *IEEE Transactions on Systems, Man, and Cybernetics, Part B: Cybernetics*, vol. 40, no. 4, pp. 1115–1127, 2010.
- [22] A. Milano, A. Priolo, A. Gasparri, M. Di Rocco, and G. Ulivi, "An experimental validation of a low-cost indoor relative position localizing system for mobile robotic networks," in *Mediterranean Conference on Control and Automation*, June 2011, pp. 169–174.
- [23] G. López-Nicolás, Y. Mezouar, and C. Sagüés, "Homography-based multi-robot control with a flying camera," in *IEEE International Conference on Robotics and Automation*, May 2011, pp. 4492–4497.
- [24] R. I. Hartley and A. Zisserman, *Multiple View Geometry in Computer Vision*, 2nd ed. Cambridge University Press, 2004.
- [25] R. T. Collins and J. R. Beveridge, "Matching perspective views of coplanar structures using projective unwarping and similarity matching," in *IEEE Conference on Computer Vision and Pattern Recognition*, 1994, pp. 240–245.
- [26] O. Faugeras, "Stratification of three-dimensional vision: projective,

- affine, and metric representations,” *Journal of the Optical Society of America A*, vol. 12, no. 3, pp. 465–484, 1995.
- [27] D. Liebowitz and A. Zisserman, “Metric rectification for perspective images of planes,” in *IEEE Conference on Computer Vision and Pattern Recognition*, June 1998, pp. 482–488.
- [28] Y. Chen and H. H. S. Ip, “Planar metric rectification by algebraically estimating the image of the absolute conic,” in *IEEE International Conference on Pattern Recognition*, 2004, pp. 88–91.
- [29] S. Mastellone, D. M. Stipanovic, C. R. Graunke, K. A. Intlekofer, and M. W. Spong, “Formation Control and Collision Avoidance for Multi-agent Non-holonomic Systems: Theory and Experiments,” *The International Journal of Robotics Research*, vol. 27, no. 1, pp. 107–126, 2008.
- [30] J. Snape, J. van den Berg, S. Guy, and D. Manocha, “The hybrid reciprocal velocity obstacle,” *IEEE Transactions on Robotics*, vol. 27, no. 4, pp. 696–706, Aug. 2011.